Comparison of measured path velocities with numerical simulations for heavily disturbed velocity distributions

Silvan Hug
Hochschule Luzern, Technikumstrasse 21, CH-6048 Horw, Switzerland
silvan.hug@hslu.ch

Thomas Staubli
Hochschule Luzern, Technikumstrasse 21,CH-6048 Horw, Switzerland
thomas.staubli@hslu.ch

Peter Gruber
Rittmeyer Ltd , CH-6340 Baar, Switzerland
peter.gruber@rittmeyer.com

Abstract
The uncertainty of an acoustic transit time (ATT) flow measurement can be estimated on the basis of computational fluid dynamics (CFD) simulations in advance of an installation. The paper illustrates an example of a flow simulation in the hydro power plant (HPP) Aratiatia, NZ, for heavily disturbed velocity distributions. In this power plant three turbines are fed from a common surge tank and are operated in parallel or individually. Details on the geometrical and numerical model are given, as well as the physical boundary conditions.
The OWICS (Optimal Weighted Integration for Circular Sections) discharge integration method at Gauss-Jacobi positions is used to calculate the flow rates in the circular measuring sections immediately upstream of the spiral casing for different operating conditions.
The procedures employed for extraction of the relevant data from the simulated flow fields needed for integration of the flow rates are described. A comparison of the axial and cross velocity components on the individual paths resulting from the CFD simulations and the measurement shows good agreement. From this agreement can be concluded that the shape of the disturbed velocity distributions as well the secondary flow is well predicted by the simulation. An analysis of the integrated path velocities show that the integration uncertainty remains below 1.3 % for the chosen 8 path, two plane configuration, even for the worst operating condition.

1. CFD Simulation

1.1. General procedure

1.1.1. Geometrical model for CFD

Basis of a reliable CFD simulation is an adequate model of the flow surfaces. This comprises:

- Definition of the simulation domain (inlet, outlet)
- The geometry must be modeled in a way that the flow predictions encompass the major influences on velocity distributions.
- Drawings of plants are often incomplete or inaccurate. Geometrical checks are necessary or as-built and approved drawings should be used.
- Simplification of the geometry is allowed (e.g. inlet trash rack, bulkhead gate slots), in case where a negligible influence on velocity distributions may be assumed.
- To enable a good meshing it is essential to set the geometrical tolerances of the CAD model to a minimum. This is especially important for transitions between different cross-sections or for edges so that the boundary layer can be accurately projected onto the geometry.
- Export of the geometry from the CAD software in a suitable format to the used meshing program.

1.1.2. Numerical models

- In general, steady state simulations will be sufficient to predict time averaged velocity distributions. However, it should be noted that bend flows, wake flows and swirling flows are inherently unsteady.
- The SST (shear stress transport) turbulence model provides in general satisfying results. Dissipation is sometimes overestimated with the SST model, leading to secondary flows which are damped out within short distances. LES, DES (large/detached eddy) models are also well suited for conduit flow predictions.
- The high resolution advection scheme assures good convergence for most simulations. High resolution adapts locally the scheme of the equation solver. In areas with high local gradients the solver uses a first order scheme and in areas with low gradients is solved in general with a second order scheme. Using the high resolution scheme ensures in most cases a stable solver process.
- Simulations with long and/or complicated geometries (cross-section changes, bifurcation, surge chambers, one of several turbines in operation, etc.) can be first simulated with an upwind scheme so that in a second step the high resolution solution converges.

1.2. Procedure chosen for the HPP Aratiatia

1.2.1. Geometrical model for CFD

The simulation domain extends from a four diameter straight section in the intake tunnel down to the spiral casings of the 3 turbines as shown in figures 1 and 2. Downstream of the surge tank the penstock separates into three pipes. After the trifurcation, the rectangular cross-section changes to the circular cross section which remains constant down to the measuring plane. The three-dimensional CAD file was prepared with UG NX 7.5, based on drawings from Mighty River Power, NZ.

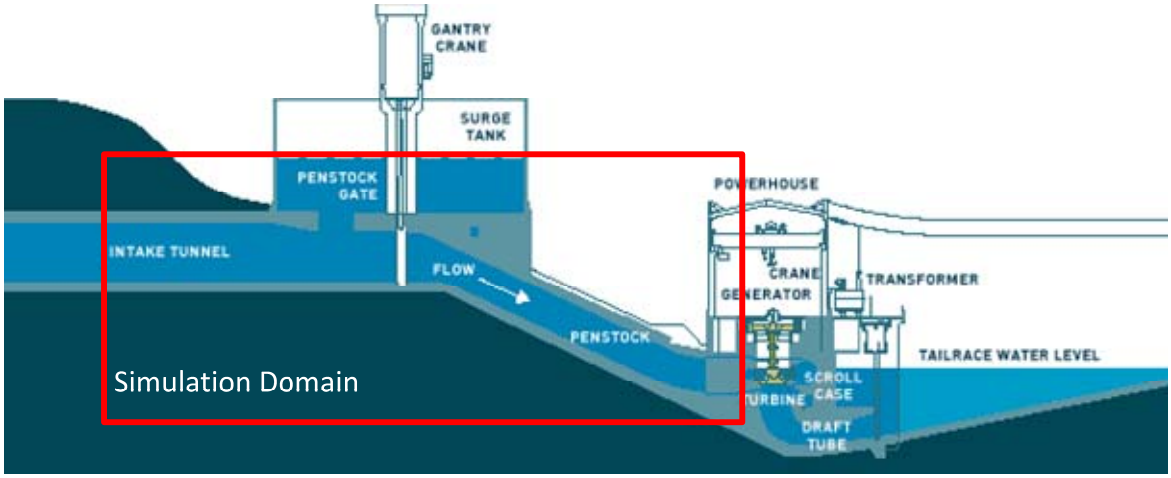

Figure 1: Simulation domain of the HPP Aratiatia

1.2.2. CFD simulation

The simulations were performed with ANSYS CFX 12.0. Figure 2 depicts the simulated flow surfaces of the HPP Aratiatia. The simulated flow measuring sections (marked as ATT) are located in the lower part of each penstock. In the following only the results of penstock 1 will be compared.

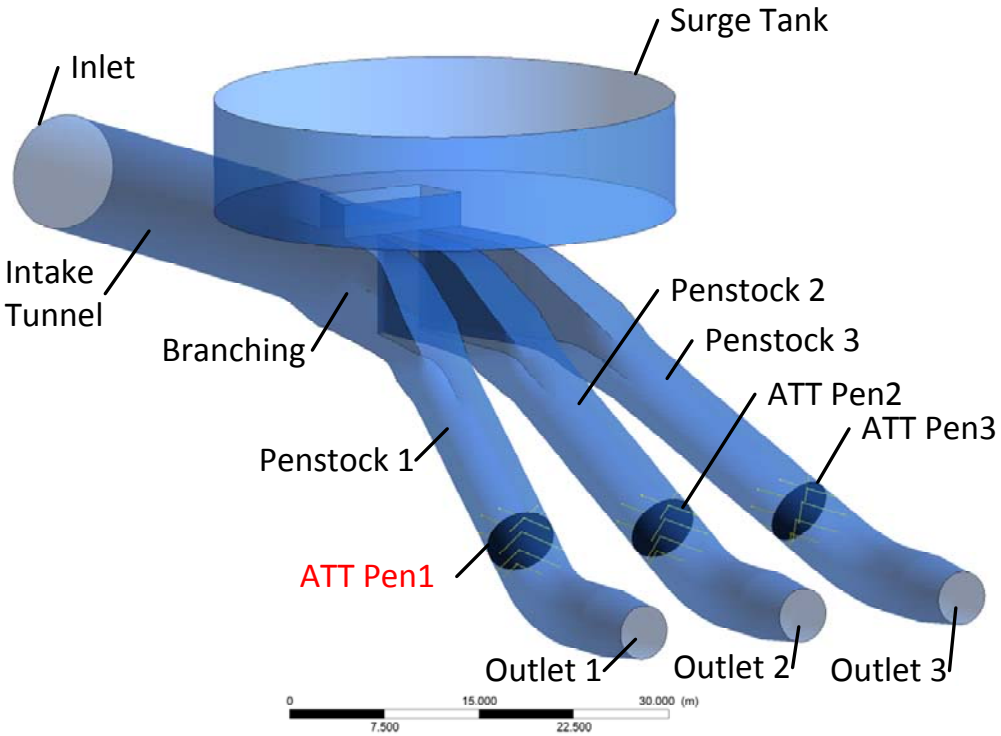

Figure 2: Overview of the parts of the simulation domain of the HPP Aratiatia

Three different operating conditions were analysed:

- Test 1: 3x90 m3/s (all three turbines in operation)
- Test 2: 2x90 m3/s (turbine 1 and 2 in operation, turbine 3 shutdown)
- Test 3: 1x50 m3/s (turbine 1 in operation, turbine 2 and 3 shutdown)

The boundary conditions for these operating points are listed below:

Inlet

The straight intake tunnel of the power plant is about 50 diameters long with constant circular cross section. The range of the Reynolds numbers lies between $Re=7 \cdot 10^6$ and $4.3 \cdot 10^7$ for the investigated operating points. Consequently, a fully developed velocity profile can be assumed at the inlet to the simulation domain. This profile is calculated beforehand for each of the given flow rates in a separate simulation with a 2 diameter short straight section with translationally periodic boundary conditions. These velocity distributions as well as the turbulence quantities are then used as inlet conditions for the main simulations.

Outlets

The number of outlets varies from 1 to 3 outlets depending on the operating conditions. The mass flow is set for each of the outlets. The outlet mass flows then are linked to the mass flow at the inlet in order to satisfy the mass flow balance.
The expressions in the brackets show the boundary conditions, which are set at the outlet.
Test 1: All three outlets have the same mass flow (*massflow@inlet/3*).
Test 2: Outlet 1 and 2 have the same mass flow (*massflow@inlet/2*). Outlet 3 is defined as a no slip wall. This is a simplification, in reality the domain ends in the spiral casing upstream of the closed guide vanes.
Test 3: Outlet 1 and inlet have the same mass flow (*massflow@inlet/1*). Outlet 2 and 3 are defined as no slip walls.

Wall

The wall is specified as a no slip wall assuming hydraulically smooth surfaces.

Free surface
The free surface of the surge tank is defined as a free slip wall. This means that the water level is constant and the water has no friction at this boundary.

2. Path velocities determined from CFD

2.1. Flow rate integration

The acoustic sensors are mounted in the three penstocks in accordance with IEC 60041 on the Gauss-Jacobi positions (table 1). Due to an expected cross-flow, the paths are arranged in two crossed planes. The paths 1 to 4 are in plane A and the paths 5 to 8 are in plane B. Two crossed paths lie on the same layer, e.g. layer 1 is defined by path 1 and 5.
The flow rate is evaluated with the position corrected OWICS weights [1]. The paths of length L_i are oriented with an angle of φ = 45° to the axial pipe direction and the projected length of the acoustic path is $L_{proj\_i} = L_i \cdot \sin(\varphi)$. With this information and the distances d_i from the centre line the co-ordinates of the start and the end point of each path was determined in the CAD-model. After modelling the paths at each level in the CAD-model, the *x*, *y*, *z* co-ordinates of each point could be copied into CFX.

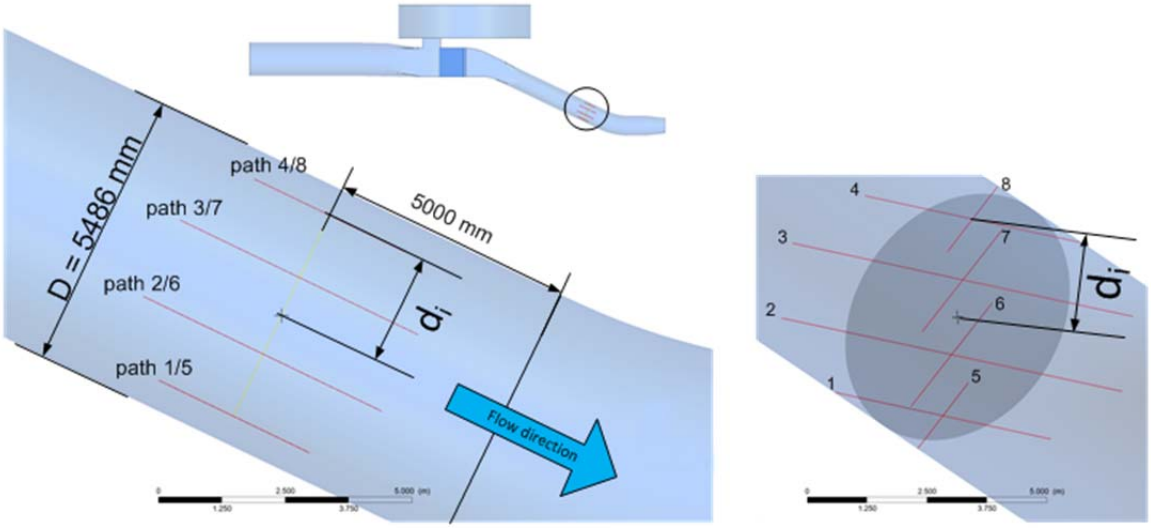

Figure 3: Path positions within the penstock 1

With a given area flow function $F(z) = \bar{v}_{ax}(z) \cdot b(z)$, the co-ordinate *z* in direction of the layers and with *b(z)* = L_{proj} the flow rate can be approximated with equation 3.1 [2]:

$$Q = \int_c^d F(z)dz = \int_c^d F(z)R(z)dz \cong \frac{D}{2}\sum_{i=1}^{N} w_i F(z_i) = \frac{D}{2}\sum_{i=1}^{N} w_i b(z_i)\bar{v}_{ax}(z_i) \qquad (2.1)$$

The area flow function used to determine OWICS weights [2] for circular cross sections is:

$$F(z) = v_{\max} \cdot D \cdot \left(1 - \frac{d(z)^2}{(D/2)^2}\right)^{\kappa} \quad \text{where } \kappa = 0.6 \qquad (2.2)$$

This area flow function bases on a ideal velocity distribution which can be approximated by:

$$v_{OWICS}(z) = v_{\max} \cdot \left(1 - \frac{d(z)^2}{(D/2)^2}\right)^{\kappa - 0.5} \qquad (2.3)$$

With the corrected OWICS weights w_i for each position, given in table 1, the flow rate Q can be determined with equation (2.4) [2].

$$Q = \frac{D}{2}\sum_{i=1}^{N} w_i \cdot \bar{v}_{ax\_i} \cdot L_{proj\_i} \qquad (2.4)$$

	Gauss-Jacobi Positions OWICS Weights	
path	Positions $d_i/(D/2)$	Weights w_i
1/5	-0.809017	0.365222
2/6	-0.309017	0.598640
3/7	0.309017	0.598640
4/8	0.809017	0.365222

Table 1: Gauss Jacobi positions and position corrected OWICS weights

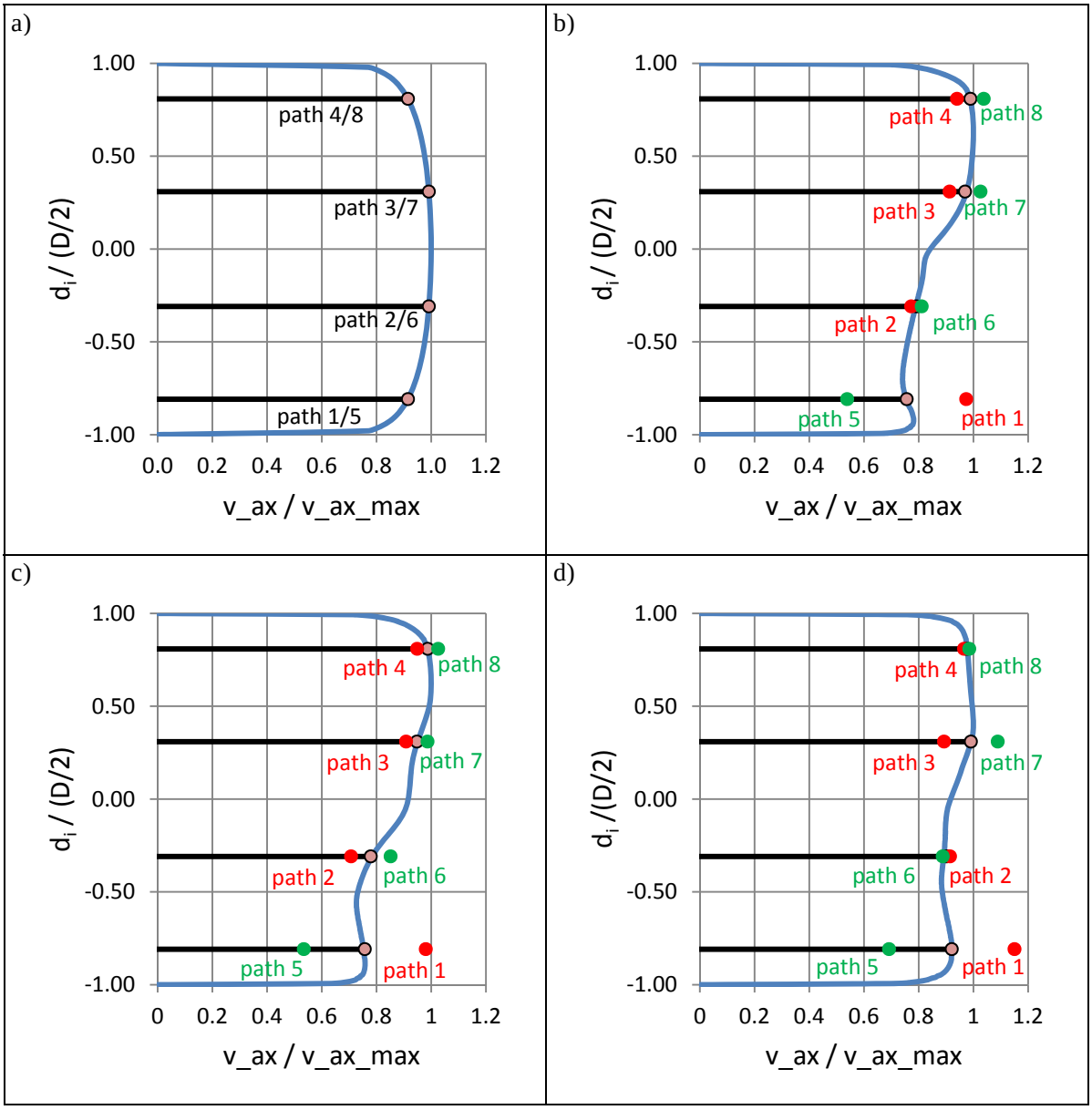

Figure 4: Normalized theoretical and simulated velocity profiles and path velocities in the penstock 1: a) OWICS velocity profile ($\kappa = 0.6$); b) test 1; c) test 2; d) test 3

Figure 4 depicts the velocity profiles of the ideal velocity distribution and of the three test cases. The black lines in figure 4 represent the Gauss-Jacobi positions d_i which are listed in table 1. The simulated axial velocity distributions (blue lines for b), c) and d)) are averages of the simulation results of plane A and plane B, deviate considerably from the ideal distribution. Furthermore, the individual points of plane A (red) and plane B (green) show an important difference of the axial velocities in the two planes.

2.2. Determination of the velocity components at the paths

For the comparison of the results of the CFD simulations with the measurements it is important that the correct axial and transversal velocity components on the virtual paths are exported from the CFD result file. Figure 5 illustrates the simple case of the velocity components without cross-flow. For the measurements v_{proj} is determined from the transit time differences of the upstream and downstream acoustic pulses. With the angle φ of the path, the mean axial flow velocity of the path can be calculated.
The extraction of the mean axial flow velocity from the CFD solution demands the export of the geometrical information (*x*, *y*, *z* co-ordinates) and the corresponding velocity components (*u*, *v*, *w*) of each point along the path.

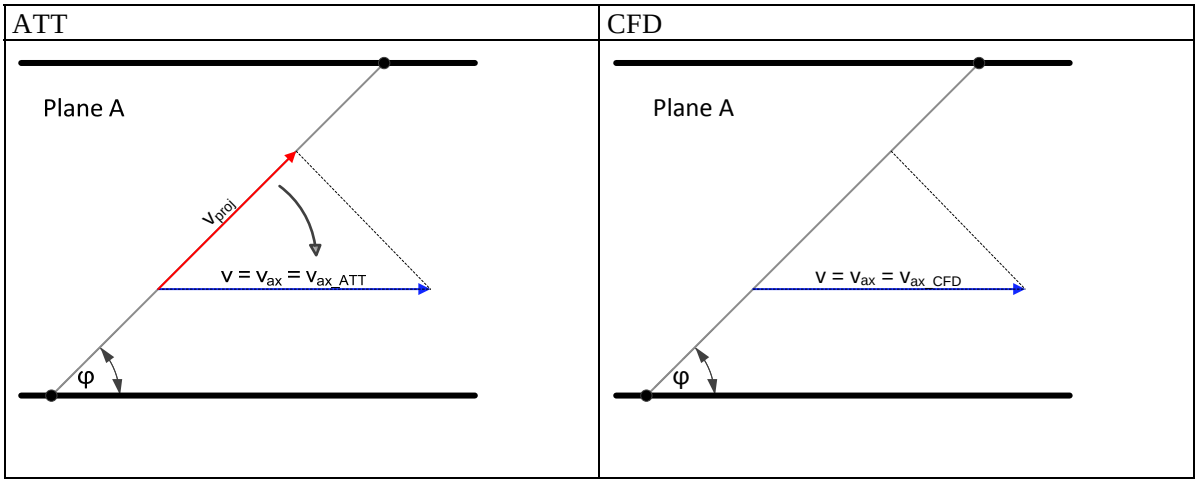

Figure 5: Comparison of the axial velocity components of the ATT-method (left) and CFD (right) without cross-flow

For the majority of applications of ATT measurements cross-flow prevails. The cross-flow affects the transit time measurement. Depending on the direction of the cross-flow, a too long or a too short transit time is measured. If both paths experience the same cross-flow, the average of the crossed transit times cancels the cross-flow effect out.
Figure 6 shows the velocity components, which affect the transit times in case of cross-flow. The velocity *v* is the real velocity of the fluid. This velocity has an axial component (v_{ax}) and a transversal component (v_{trans}). As the figure shows, v_{proj} is larger on plane A than on plane B. This is because v_{trans} increases the transit time of the pulse on plane A while v_{trans} decreases on plane B. For the comparison of the CFD results with the measured data it is important that the cross-flow component is also considered.

1. Export of the geometrical information (*x*, *y*, *z* co-ordinates) and the corresponding velocity component (*u*, *v*, *w*) of each path.
2. Calculation of the mean velocities of each component (*u*, *v*, *w*) with the trapezoidal rule.
3. Calculation of v_{ax} and v_{trans}
   v_{ax}: the axial velocity component is directed in the axial flow direction.
   v_{trans}: the transversal velocity component is directed normally to the axial velocity component and is located on a layer.
4. Calculation of v_{ax_proj} and v_{cross}

$$v_{ax\_proj} = v_{ax} \cdot \cos(\varphi) \tag{2.5}$$

$$v_{ax\_cross} = v_{trans} \cdot \sin(\varphi) \tag{2.6}$$

5. Calculation of v_{proj}

   Plane A: $v_{proj} = v_{ax\_proj} + v_{cross}$ (2.7)

   Plane B: $v_{proj} = v_{ax\_proj} - v_{cross}$ (2.8)

6. Calculation of v_{ax_CFD}

   Plane A: $v_{ax\_CFD} = \frac{v_{proj}}{\cos(\varphi)} = v_{ax} + v_{trans} \cdot \tan(\varphi)$ (2.9)

   Plane B: $v_{ax\_CFD} = \frac{v_{proj}}{\cos(\varphi)} = v_{ax} - v_{trans} \cdot \tan(\varphi)$ (2.10)

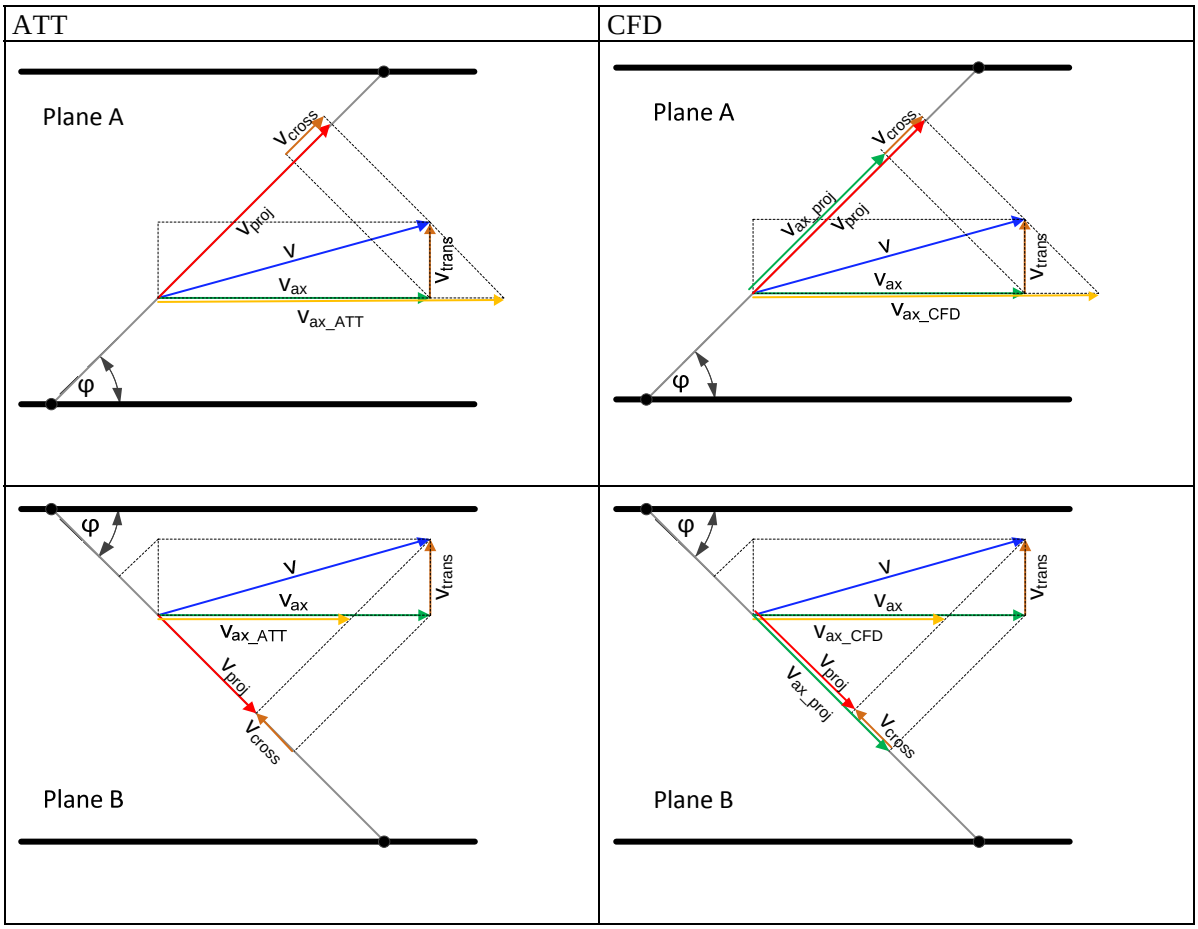

Figure 6: Comparison of the velocity components of the ATT-Method and CFD with cross-flow

2.3. CFD results

All results are referenced to a specified volume flow of *90 m^3/s* respectively of *50m^3/s*. The table 2 shows the relative deviations of the flow rates integrated with the OWICS (Gauss-Jacobi positions) method and the CFD flow rate, which is determined from the mass flow given in the CFD result file. The deviation e_{OWICS} (2.11) results from average of the flow rates from plane A and plane B. In the worst case (test 2) the integration error of the OWICS method results to *-1.21 %*. The other two simulations show an integration error below *1 %*. The smallest deviation is found for the simulation with all penstocks in use (test 1).

The deviations of plane A and plane B are not identical. On the one hand cross-flow will be one of causes for this difference, but on the other hand the integration error of the OWICS method will also be different due to the difference of the disturbed velocity distributions in Plane A and B.

	2 planes (A and B) with each 4 paths			
Case	**Q_CFD** [m^3/s]	**e_owics** [%]	**e_plane_A** [%]	**e_plane_B** [%]
Test 1: 3x90 m^3/s				
Penstock 1	90	0.79%	0.28%	1.29%
Test 2: 2x90 m^3/s (Pen 1&2)				
Penstock 1	90	-1.21%	-2.94%	0.53%
Test 3: 1x50 m^3/s				
Penstock 1	50	0.90%	0.83%	0.97%

Table 2: Results of the flow rates with the OWICS (Gauss-Jacobi positions) method in the penstock 1

$$e_{OWICS} = \frac{Q_{OWICS} - Q_{CFD}}{Q_{CFD}} \tag{2.11}$$

$$e_{plane\_A} = \frac{Q_{plane\_A} - Q_{CFD}}{Q_{CFD}} \tag{2.12}$$

$$e_{plane\_B} = \frac{Q_{plane\_B} - Q_{CFD}}{Q_{CFD}} \tag{2.13}$$

It should be noted that the integration error is only part of the uncertainty of the ATT method. Further uncertainties such as the uncertainties due to protrusion, installation and electronics have also to be considered.

3. Acoustic transit time measurement in the HPP Aratiatia

3.1. Measurement

During the tests in the HPP the Aratiatia the specified flow rates where reached as close as possible. Each test consisted of a *5-10* minutes stabilisation period, followed by a *5* minutes data acquisition period. The sampling frequency was set to *1* s^{-1}. For test 1 and 2 the flow rate was almost constant at *90* m^3/s during the entire measuring period of *300 s*. The standard deviation were $\sigma = 0.999\ m^3/s$ for test 1 and $\sigma = 0.807\ m^3/s$ for test 2.
Test 3, with a specified flow rate of *50* m^3/s, shows a flow rate increase in between *75 s* and *150 s*. Accordingly, the time mean flow rate was determined for sequence between *150 s* and *300 s* for this test 3. The standard deviation of the time signal of test 3 was $\sigma = 0.574\ m^3/s$.

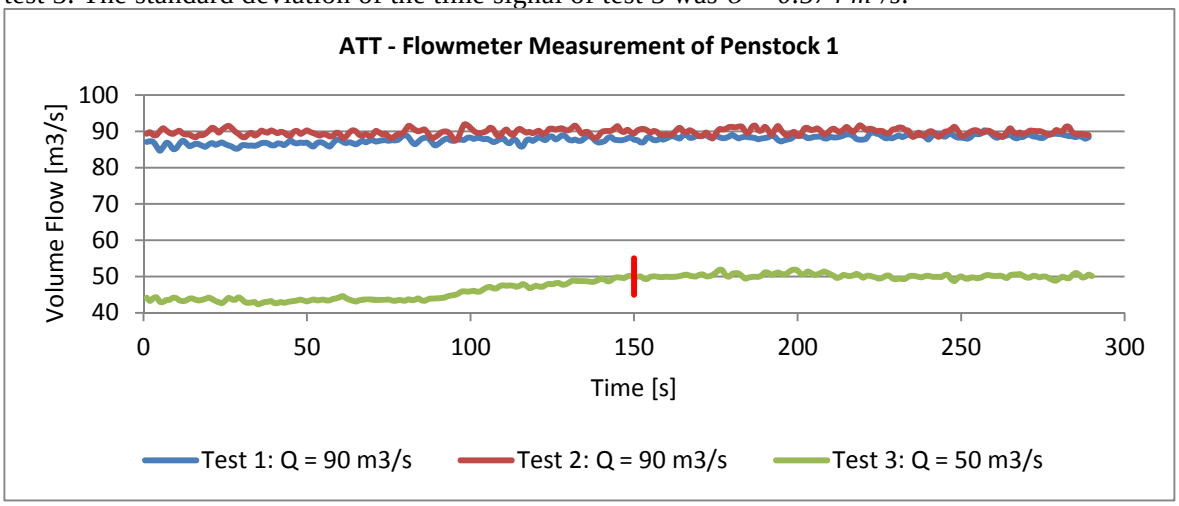

Figure 7: Flow rate recordings for the three different tests in penstock 1

4. Comparison of measured and simulated path velocities

4.1. Path velocities

The figures 8 to 10 show the measured axial velocity components (v_{ax_ATT}) and the simulated axial velocity components (v_{ax_CFD}) for each path (P1 to P8). Between the measured and the simulated data the ideal axial velocity is inserted in order to demonstrate the important profile distortion in the measuring section. All values are specified to the volume flow of *90 m^3/s* respectively to *50 m^3/s*.

Measured path velocities and simulated velocities agree fairly well with each other. For test 1 the maximum deviation between ATT measurement and CFD is only for P5 of the order of *10 %* all other deviations are smaller. For test 2 the largest deviations are found for P5 and P8. The deviations of test 3 are more significant and peak for P1 with *17%*.

Comparing velocities in plane A (P1, P2, P3, P4) and plane B (P5, P6, P7, P8) considerable differences are observed, indicating heavily disturbed velocity distributions and cross-flow.

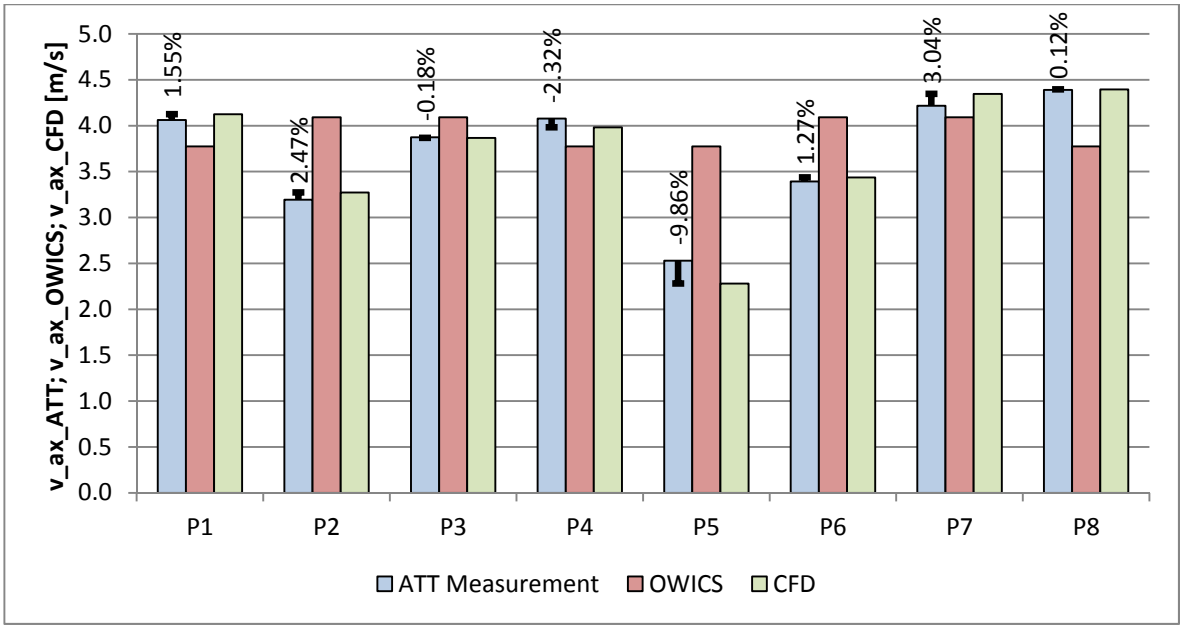

Figure 8: Comparison of the axial velocities for test 1 in penstock 1

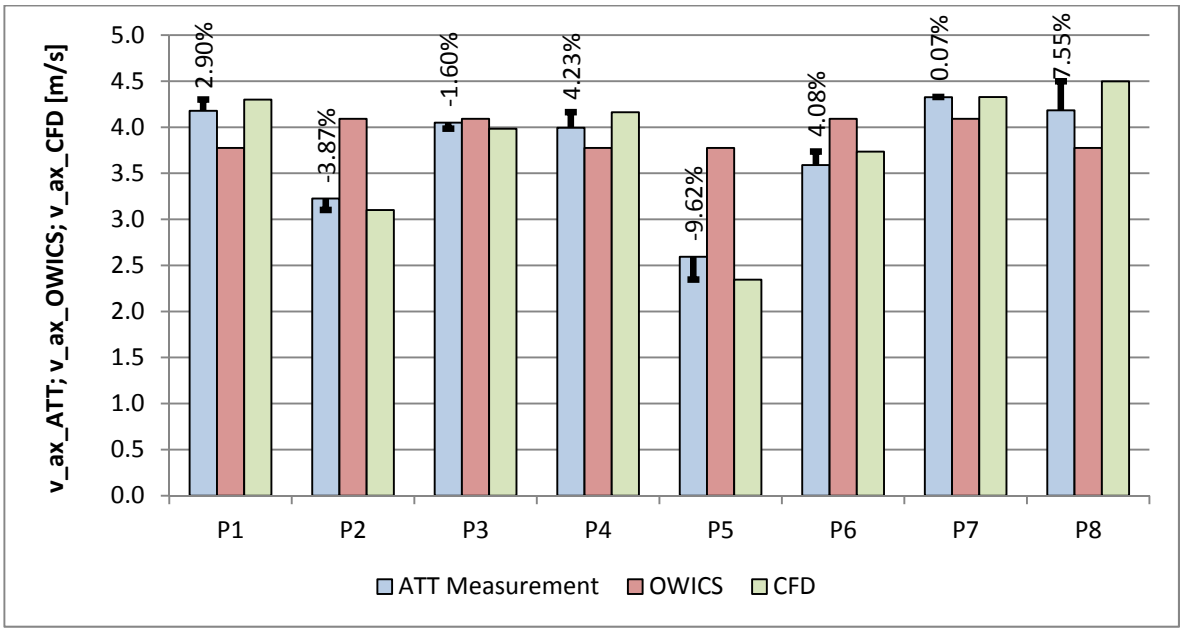

Figure 9: Comparison of the axial velocities for test 2 in penstock 1

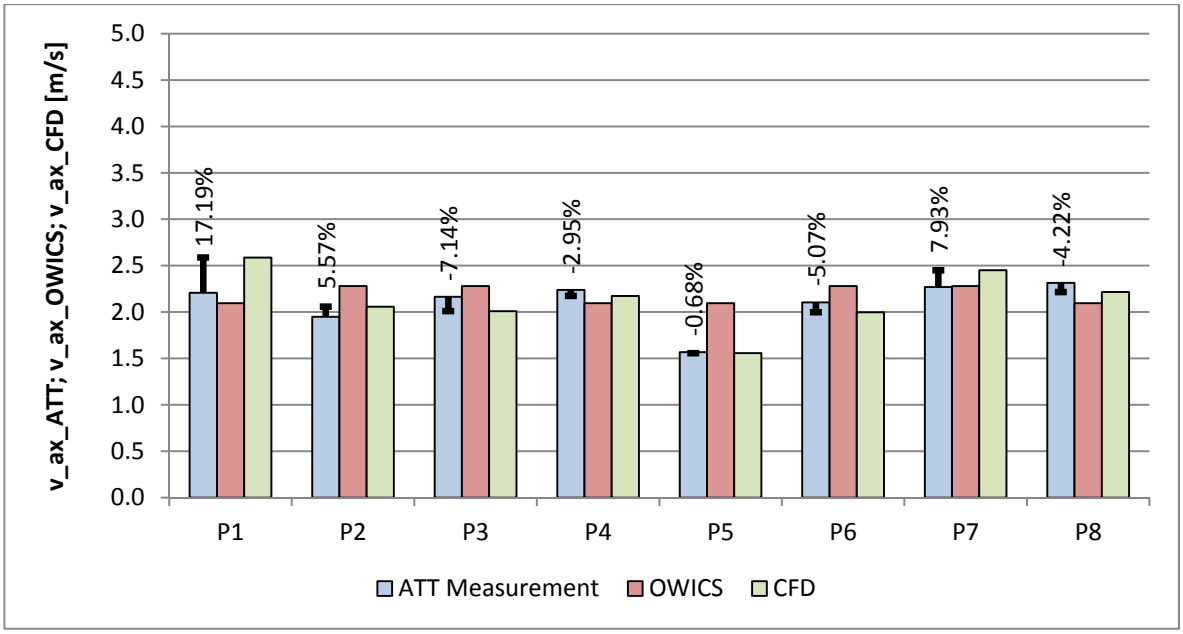

Figure 10: Comparison of the axial velocities for test 3 in penstock 1

The figures 11 to 13 show the mean axial velocity (left) and the transversal velocity (right) in the layers 1 to 4. The maximum deviation of the mean axial velocity between the measured and the CFD results of a layer amounts to less than *10%* at all cases. The majority of the deviations are near *3%* and smaller. The deviations of the transversal velocity are larger than the deviations of the axial velocity components. The sign of the transversal velocity components is well predicted, with the exception on layer 2 for test 3, with very small cross-flow. The transversal velocity components are slightly over predicted by CFD. The cross-flow of the ideal velocity distribution is obviously zero. For all 3 tests, the highest transversal velocities are found on layer 1.

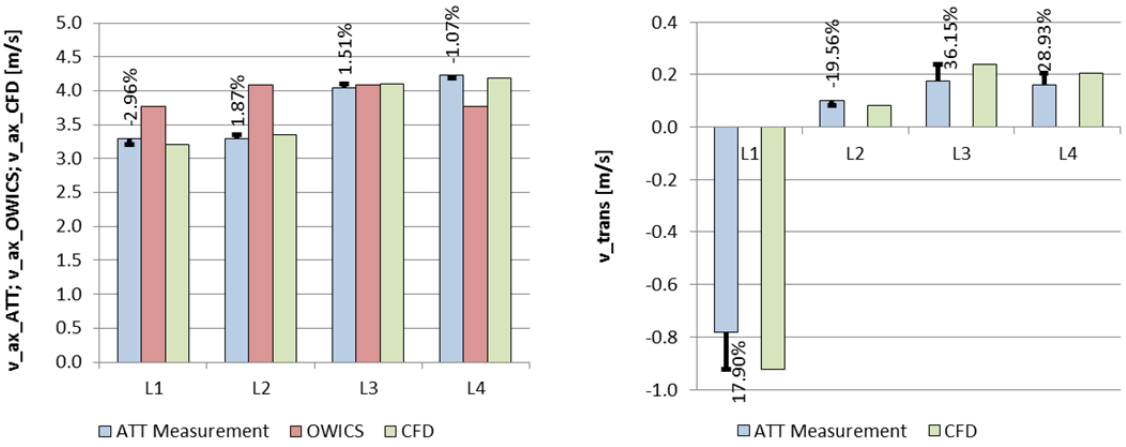

Figure 11: Comparison of the axial and the transversal velocities on the 4 layers of test 1 in penstock 1

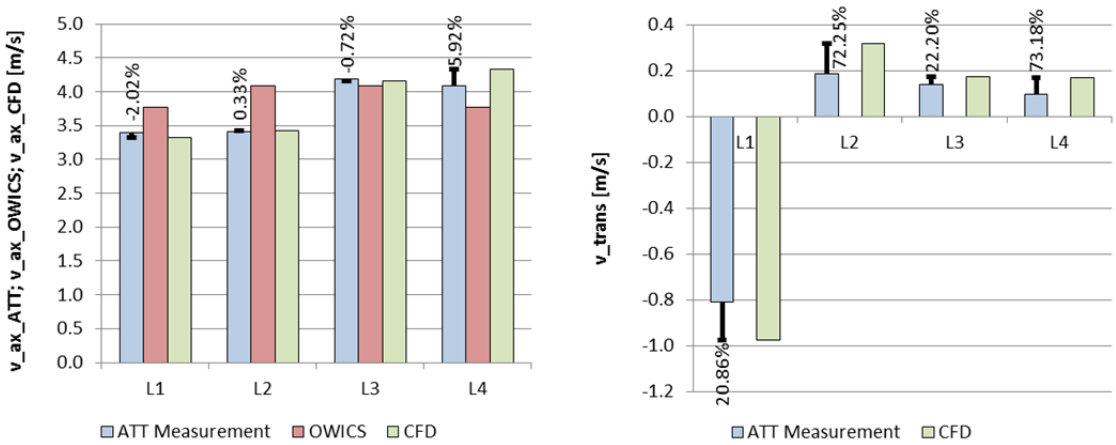

Figure 12: Comparison of the axial and the transversal velocities on the 4 layers of test 2 in penstock 1

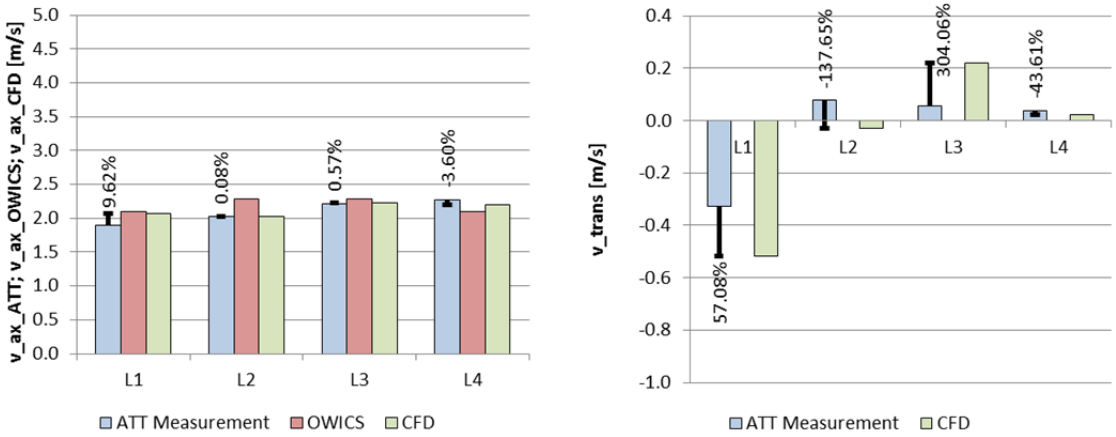

Figure 13: Comparison of the axial and the transversal velocities on the 4 layers of test 3 in penstock 1

In Figure 14 the secondary flow, which is developing downstream of the trifurcation, is shown in 3 consecutive planes. It is this secondary flow which is responsible for the transverse velocity components on the acoustic paths. The colour from blue to red indicates the magnitude of the transverse velocity component in the cutting plane. The red zone in the lower part of the penstock shows the location of maximum secondary flow. Also located in the lower part of the penstock is the core of the counter rotating vortex with very low transverse velocities in the centre. The three consecutive cuts show that the whole system of the secondary flow is in rotation itself. This can be observed in the area with the highest velocities and also from the rotation of the vortex core. Further observation is that the intensity of the secondary flow decreases along the penstock. The negative transverse velocities in figures 11 to 13 on layer 1 correlate well with the high velocities from left to right at the height of this layer depicted in figure 14. On all other layers a transverse flow from right to left dominates.

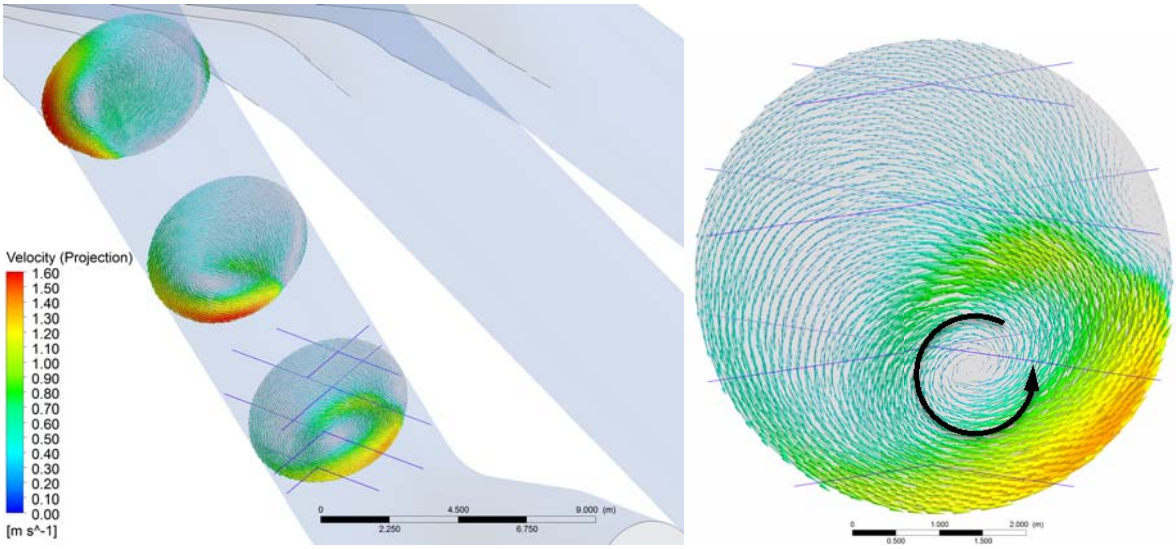

Figure 14: Projected velocity vectors of test 1 in penstock 1 on 3 consecutive planes (left) and on the measuring plane (right)

5. Conclusion

The flow in the penstocks of the hydro power plant Aratiatia has been simulated for 3 operating points. Due to the trifurcation, the cross-section change and the bends, the velocity profile at the ATT measuring section is heavily disturbed and a cross-flow prevails. Uneven distributions and cross-flow, both, affect the accuracy of flow rate integration.

For reliable CFD simulations, it is important, that the correct boundary conditions are set and only low impact simplifications are made to the geometry.

The flow rate integration of the simulated velocities with the OWICS method at the Gauss-Jacobi positions shows that in the measurements an integration uncertainty of less than *1.3%* has to be expected. The comparison of the measured and simulated mean axial and transverse velocities on the acoustic path show reasonably good agreement from what can be concluded that the predicted integration uncertainty is correct.

6. References

[1] Voser A. „Analyse und Fehleroptimierung der mehrpfadigen akustischen Durchflussmessung in Wasserkraftanlagen“, PhD thesis, ETH Zürich, 1999

[2] Tresch T. et al., “Presentation of optimized integration methods and weighting corrections for the acoustic discharge measurement”, IGHEM 2008, Milano